

# Experimental Study on the Physical Properties of Iron Ore Granules Made from Australian Iron Ores

Chengzhi LI,<sup>1)</sup> Roberto MORENO-ATANASIO,<sup>2)</sup> Damien O'DEA<sup>3)</sup> and Tom HONEYANDS<sup>1)\*</sup>

1) Centre for Ironmaking Materials Research, School of Engineering, The University of Newcastle, Callaghan, NSW, 2308 Australia. 2) Chemical Engineering Department, School of Engineering, The University of Newcastle, Callaghan, NSW, 2308 Australia. 3) BHP, 480 Queen St, Brisbane, QLD, 4000 Australia.

(Received on July 17, 2018; accepted on October 15, 2018; J-STAGE Advance published date: December 5, 2018)

A fundamental experimental study was conducted to measure the physical properties of iron ore granules made from three types of Australian iron ores. In this study, some key physical property parameters, including apparent density, Young's modulus and the coefficients of static and rolling frictions, of the iron ore granules with varying moisture content were investigated. The effect of granule size on the considered property parameters was also studied for the iron ore granules at the optimal moisture content which was determined by permeability pot packing test. The measurement results showed that both apparent density and Young's modulus of iron ore granules generally decreased with moisture content due to the growth of adhering layer around the nuclei particles. The static friction coefficient generally increased with moisture content but, at lower moisture contents, its variation differed between the granule types. The rolling friction coefficient generally experience a minimum value as moisture content increased within the considered range. The moisture content for the minima varied with granule type due to the different characteristics of the ore types. At the optimal moisture content for each granule type, the apparent density of different granule size fractions showed variable values because of the heterogeneous composition of the raw mixture in each size fraction. The Young's modulus and static friction coefficient showed slight downward and upward trends with the increase of granule size, respectively. The rolling friction coefficient is nearly independent of granule size.

KEY WORDS: iron ore granule; physical properties; moisture content; granule size; iron ore.

## 1. Introduction

In the recent two decades, rapid economic growth in Asian-Pacific region has spectacularly boosted the global steel industry. To meet ever-increasing demand of iron raw materials, the global iron ore production (usable iron ore) has increased from about 970 Million tons to about 2.3 Billion tons between 2000 and 2015.<sup>1)</sup> Australia is currently the world's largest exporter of iron ore and is responsible for nearly half of all iron ore exports in the past five years. For over two decades now, the major iron ore products developed in Australia have included hematite ores (*e.g.* Brockman) and hematite-goethite ores (*e.g.* Marra Mamba ores and Channel Iron Deposit ores) with a relatively higher grade of combined water. Nowadays, these products have obtained a considerable market share of global iron ore trade and accounted for a significant component of sintering blends particularly in most Asian steel plants.<sup>2)</sup> Since these products have a wider range of grades, sizes and mineral types compared to historical ores, it is important for iron-makers to understand the conditions required for effective granulation to optimise the behaviour of the produced iron ore granules during the sintering process.

In the preparation stage of sintering, the iron ores, mixed with coke breeze, fluxes and return sinter particles, are sub-

jected to a granulation process in which the material mixture is agglomerated with moisture into iron ore granules. The principal mechanism of the iron ore granulation is called "auto-layering"<sup>3,4)</sup> in which the fine size components of the mixture adhere to the surface of the coarser particles of the mixture due to the capillary forces.<sup>5)</sup> As a result of the auto-layering process, the iron ore granules generally have a structure of an inner nucleus particle and an outer adhering layer (as shown in Fig. 1). Subsequently, the iron ore granules, with a narrow size distribution and proper strength, are packed onto the moving pallets for sintering. The behaviour of iron ore granules during this charging process is considered a key factor in sintering because it determines the structural properties of the packed bed. For

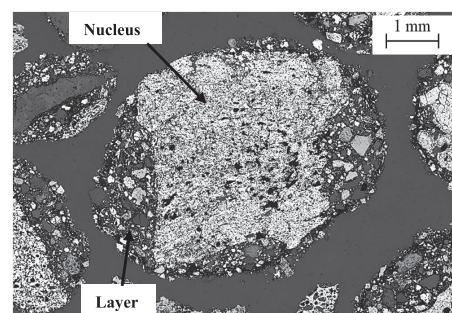


Fig. 1. Micrograph of the structure of typical iron ore granules.

\* Corresponding author: E-mail: tom.a.honeyands@newcastle.edu.au  
DOI: <https://doi.org/10.2355/isijinternational.ISIJINT-2018-508>

instance, the bed permeability, as a function of mean granule size and packing voidage, can significantly influence the air flow rate and the flame front speed, which are very important for sintering productivity.<sup>6)</sup>

Due to the importance of granule behaviour in sintering, many studies have been carried out on this topic in recent years<sup>7,8)</sup> Considering that the behaviour of iron ore granules was too complicated to be experimentally studied in detail, many researchers<sup>9-15)</sup> turned to numerical tools, such as Discrete Element Method (DEM), to investigate the granule behaviour in their studies. However, one existing issue is how to determine the physical parameters of the simulated iron ore granules because these parameters vary with moisture content and ore type. Considering the fact that rare references on the physical properties of iron ore granules have been published so far, it is necessary to determine the values of the key physical parameters of iron ore granules via experimental measurements. Therefore, to fill the gap in this area, a systematic study of the physical properties of iron ore granules at different moisture contents is required.

Many experimental approaches to measure particle physical parameters have been reported by earlier researchers. Since 1960s, Jenike shear cell<sup>16)</sup> and ring shear cell<sup>17)</sup> were applied to the measurement of the Coulomb friction between bulk solids or between bulk solids and wall materials. However, these testers are not applicable to large particles (normally +4 mm) and this restricts their application to the measurement of iron ore granules. Because of this drawback, some new methods<sup>18,19)</sup> were invented to measure the friction coefficient between large particles such as iron ore pellets (+9 mm). However, these methods are relatively complex to prepare and thus may not be very cost-efficient for laboratory experiments. The apparent particle density was commonly measured via the fluid displacement method<sup>5,20)</sup> in which the apparent density was calculated as the ratio of the particles' mass to the volume of the fluid (usually water or kerosene) displaced by the soaked particles. Wang *et al.*<sup>19)</sup> measured the elasticity of individual iron ore pellets using a compression test where the elastic modulus of pellet was calculated based on the relationship between pressure force and pellet indentation. Doménech *et al.*<sup>21)</sup> and Ai *et al.*<sup>22)</sup> respectively proposed the methods of measuring the coefficient of rolling friction of a particle placed on a ramp but the former method is specifically for spherical particles. In summary, for these existing measurement methodologies, we made some modifications to the methods which are generally feasible for the parameter measurements of iron ore granules, aiming to make them more suitable for testing iron ore granules. The detailed modifications for each applied method are described in the following section on experimental methodologies.

In this work, three types of single Australian iron ores

were granulated in the experiments, along with a fixed proportion of fluxes, coke and return fines. The measurements of some key physical property parameters of the iron ore granules, including apparent density, Young's modulus and the coefficients of static and rolling frictions, with varying moisture content were systematically investigated. Furthermore, the effect of granule size on the considered property parameters of the granules at the optimal moisture content was also studied for each granule type. These experimental data are expected to provide more information of iron ore granules for future researchers.

## 2. Preparation Work

### 2.1. Iron Ore Characteristics

**Table 1** shows the dry size distribution and initial moisture content  $W_{IMC}$  of the iron ores studied in this work. Ores A, B and C are hematite, Brockman - Marra Mamba and Channel Iron Deposit iron ores, respectively. The data show that Ores A and B have obviously higher fine size component (-0.25 mm) than Ore C. In turn, Ore C has a higher coarse size component (+1.0 mm), especially the larger particles (+5.6 mm), than the other two ore types. The initial moisture of Ore A is relatively lower than those of Ores B and C. This indicates that compared with the other two ore types, the material mixture containing Ore A requires more water to obtain the same target granule moisture in the granulation process.

The iron ore particle characteristics, including sphericity, apparent density, porosity and water holding capacity (WHC), were investigated in the preparation work. The sphericity of ore particles was measured according to Wadell's method.<sup>23)</sup> The apparent density of ore particles was measured based on fluid displacement method.<sup>5)</sup> The particle porosity was calculated as a function<sup>24)</sup> of the apparent density and the skeletal density measured by a gas pycnometer. The water holding capacity (WHC) of ore particles were measured<sup>24,25)</sup> based on the mass difference between saturated and dried particle samples.

**Table 2** shows the chemical composition, sphericity  $\phi$ , apparent density  $\rho_a$ , porosity  $P$  and water holding capacity (WHC) of the studied ores. The information of chemical composition indicate that hematite Ore A has a higher Fe grade than the other two ore types and has the lowest LOI (loss on ignition) content. In contrast, Channel Iron Deposit Ore C has the highest LOI content and hence the lowest Fe grade. Brockman - Marra Mamba Ore B has a moderate LOI content and consequently an intermediate level of Fe grade. The sequence of ore particle sphericity is Ore C > Ore A > Ore B. This indicates that Ores A and B have generally less-round appearances and Ore C is relatively rounder than the former ore types. Ores A has the densest structure and the

**Table 1.** Size distribution and initial moisture of the studied iron ores (mass%).

Name	Ore type	Cumulative mass% passing (mm, dry basis)									$W_{IMC}$
		8.0	5.6	4.0	2.8	2.0	1.0	0.50	0.25	0.125	
A	Hematite	96.1	84.4	70.6	60.6	51.9	37.8	27.2	16.9	9.2	4.6
B	Brockman - Marra Mamba	93.5	80.9	69.2	61.6	53.5	42.4	34.2	20.3	10.7	6.2
C	Channel Iron Deposit	88.0	77.9	69.3	60.5	49.3	30.5	15.4	5.7	2.8	6.4

**Table 2.** Summary of the characteristics of studied iron ores.

Name	Chemical composition (wt.%)						$\phi$	$\rho_a$ (g/cm <sup>3</sup> )	$P$	WHC (%)
	TFe	SiO <sub>2</sub>	CaO	Al <sub>2</sub> O <sub>3</sub>	MgO	LOI				
A	62.64	4.35	0.09	2.29	0.09	3.28	0.820	3.76	0.212	6.06
B	60.74	4.44	0.04	2.20	0.05	5.79	0.803	3.38	0.250	8.82
C	57.17	5.72	0.06	1.34	0.09	10.40	0.865	3.05	0.235	8.04

The sphericity, apparent density, porosity and water holding capacity were measured using coarse particles of size fraction -4.0+2.0 mm.

lowest porosity of the studied ore types. The values of WHC are in the same order with that of porosity.

### 2.2. Granulation Procedure

The iron ore granulation was conducted, following the procedure outlined by Ellis *et al.*,<sup>26)</sup> in a laboratory-scale rotary drum with a diameter of 500 mm and a depth of 310 mm. During the granulation process, each type of iron ore was mixed with coke breeze, fluxes (*e.g.* limestone and dolomite) and return sinter fines (size < 5 mm), and then agglomerated in the drum into iron ore granules. The size distributions of the additional feeding components are shown in **Table 3**. **Table 4** shows the summarised information of all the components of the material mixture. The rotation speed of the drum was kept at 20 rev/min, which corresponded to a Froude number of 0.0045. The space filling degree was about 13% based on the charge mass (15 kg) for each batch of granulation. Once charged into the drum, the mixture was first pre-mixed for 2 minutes and then a certain amount of water (calculated by the difference between the initial moisture of the mixture and the target moisture content) was added to the drum via a pipe sprinkler. The time for adding water was 2 minutes and then the materials were further granulated for 6 minutes.

After granulation, the iron ore granules were carefully collected from the drum and quickly divided by rotary sample divider into several sub-samples for the subsequent measurements. These sub-samples were then sealed in air tight bags to prevent further moisture loss. The iron ore granules made from Ore A, B and C were named as Granule A, B and C, respectively. For each granule type, in total six levels of target moisture content, ranging from 7.0% to 9.5% with an interval of 0.5%, were considered in this study. However, due to the inevitable moisture loss during granule handling, the actual moisture content was usually lower than the target value by 5%–10%.

### 2.3. Optimal Moistures for Iron Ore Granule Types

The permeability tests were conducted in a JPU (Japanese Permeability Unit) pot with a diameter of 100 mm and the height of 600 mm for each iron ore granule type to determine the optimal moisture content  $W_{opt}$  at which the granule bed has the maximum permeability.<sup>26)</sup> With the optimal moisture content, the study of the influence of granule size on the physical property parameters could be simplified by focusing on the iron ore granules at the optimal moisture content which is more relevant to sinter plant operation instead of a broad moisture range. The detailed measurement procedures were referred from the previous experimental studies.<sup>27–29)</sup> In brief, based on the permeability results, the  $W_{opt}$  for Gran-

ules A, B and C were determined as 7.15 wt.%, 8.54 wt.% and 8.06 wt.%, respectively.

## 3. Measurement Procedure for Iron Ore Granules

### 3.1. Mass Ratio of Adhering Layer to Nuclei Particles

As an important index of evaluating iron ore granules, the mass ratio of adhering layer to nuclei particles,  $R_m$ , was measured for the studied iron ore granule types to help analyse the following measurement results of the studied granule property parameters. In the experiment, about 50 g of +1.0 mm granules of each moisture group were randomly collected and screened into six size fractions (*i.e.* 1.0–2.0 mm, 2.0–2.8 mm, 2.8–4.0 mm, 4.0–5.6 mm, 5.6–8.0 mm and +8.0 mm). The sample granules of six size fractions were respectively put in six marked beakers. Then the beakers were put in oven and dried at 105°C for 24 hours. The dried granules of each size fraction were first weighed and then washed over the corresponding next smaller size screen. The particles remaining on the screen were considered as nuclei particles which were then dried and weighed again. The mass of adhering layer was determined as the mass difference between the dried granules and the dried nuclei particles.

### 3.2. Sphericity of Iron Ore Granules

Granule sphericity is a measure of granule shape and it correlates<sup>22)</sup> with the coefficient of granule rolling friction. The sphericity of the studied iron ore granules with varying moisture content was measured by a 3D laser scanner (Matter and Form Desktop). In the experiments, twenty iron ore granules larger than 2.0 mm (to ensure the scanning precision) were randomly selected from each moisture group of the granule samples. In one test, a single granule was put onto the scanner platform. As scanning proceeded, the information of the granule profile was collected and then converted into a 3D image by the corresponding scanning software. In theory, a complete 3D image of a granule requires at least two scanning tests because the top and bottom parts of the granule cannot be fully scanned in the first test. In this experimental work, each sample granule was scanned along three dimensions to ensure that a complete granule 3-D image could be obtained after image combination.

The complete 3D image of the tested granule was then imported to the image processing software MeshLab ([www.meshlab.net](http://www.meshlab.net)), so that the volume and surface area of the tested granule could be calculated. Hence, the sphericity of the tested granule was determined as the ratio of the surface area of a sphere which has the same volume with the tested granule to the real surface area of the tested granule, which is expressed as:<sup>23)</sup>

$$\phi = \frac{A_{\text{sphere}}}{A_{\text{granule}}} = \frac{\pi D_{\text{sphere}}^2}{A_{\text{granule}}} = \frac{\pi^{\frac{1}{3}} (6V_{\text{granule}})^{\frac{2}{3}}}{A_{\text{granule}}} \dots\dots\dots (1)$$

where  $\phi$  is granule sphericity;  $A_{\text{sphere}}$  and  $D_{\text{sphere}}$  are the surface area and diameter of the sphere which has the same volume with the tested granule, respectively (mm<sup>2</sup>, mm); and  $A_{\text{granule}}$  and  $V_{\text{granule}}$  are the real surface area and volume of the tested granule, respectively (mm<sup>2</sup>, mm<sup>3</sup>).

### 3.3. Apparent Density of Iron Ore Granules

The apparent density of iron ore granules was measured using a peanut oil displacement method. Compared with water, peanut oil is more viscous and thus can avoid more fluid penetrating into the sample granules during the soaking process. For each moisture group, about 200 g of iron ore granules with full size distribution was first evenly split into four portions for replicate measurement tests. In each test, the granules were first weighed and then soaked in a peanut oil bath for one minute. The purpose of this step was to ensure that the open pores of the granules had been filled and the channels linking to the inner parts of the granules

**Table 3.** Size distributions of the additional feeding components of the mixture (mass%).

Component	Cumulative mass% passing (mm, dry basis)							
	5.6	4.0	2.8	2.0	1.0	0.50	0.25	0.125
Return sinter	100.0	68.7	38.6	32.5	10.3	5.0	1.9	0.5
Coke breeze	100.0	95.7	85.6	75.3	55.1	42.3	30.0	19.4
Limestone	96.5	90.4	77.9	71.3	62.9	50.8	36.2	23.7
Dolomite	82.6	69.0	49.4	42.5	26.5	17.3	13.4	11.3

**Table 4.** Summarised information of all the mixture components.

Component	Mass fraction (wt.%)	$W_{IMC}$ (wt.%)	$\rho_a$ (g/cm <sup>3</sup> )
Iron ore (A/B/C)	61.2	4.6/6.2/6.4	3.76/3.38/3.05
Return sinter	20.0	0.1	3.51
Coke breeze	5.9	10.2	1.29
Limestone	8.5	0.3	2.38
Dolomite	4.4	4.0	2.45
Mixture	100.0	3.7/4.7/4.9	3.13/2.96/2.80

had been blocked by the oil. Hence, no more oil would penetrate the granules in the following oil soaking process. After oil bath, the granules were spread out on absorbent paper to remove the oil remaining on the granule surface. The wiped granules were reweighed and then placed in a 250-mL volumetric flask of known mass. The flask was then filled with peanut oil again and weighed on the balance. The apparent density of the tested granules was calculated by the following expression:

$$\rho_a = \frac{m_{gran}}{V_{flask} - V_{oil}} = \frac{m_{gran}}{V_{flask} - \frac{m_{filled} - (m_{flask} + m_{soaked})}{\rho_{oil}}} \dots (2)$$

where  $\rho_a$  and  $m_{gran}$  are the apparent density and mass of the tested granules, respectively (g/cm<sup>3</sup>, g);  $m_{flask}$  and  $V_{flask}$  are the mass and volume of the volumetric flask, respectively (g, mL);  $V_{oil}$  is the volume of the oil filled in the flask (mL);  $m_{filled}$  is the mass of the flask containing oil and granules (g);  $m_{soaked}$  is the mass of the soaked granules after oil bath (g);  $\rho_{oil}$  is the density of peanut oil at the ambient temperature (g/cm<sup>3</sup>), which was measured before the experiment started. An average value of the four replicate measurement results was finally obtained and used for data analysis.

To investigate the relationship between apparent density and granule size for the granules at the optimal moisture content, the sample granules of each ore type were sieved into four size fractions of +5.6 mm, +2.8–5.6 mm, +1.0–2.8 mm and –1.0 mm. For each granule size fraction, the granules were split into four portions and the measurement for each portion was conducted based on the procedures mentioned above. The average value of the four replicate measurement results was used for data analysis.

**3.4. Young’s Modulus of Iron Ore Granules**

The Young’s modulus of iron ore granules is a measure of granule stiffness. In this study, Young’s modulus was estimated by applying the Hertz contact law<sup>30)</sup> which is a classic theory established for analysing the contact of two elastic solids. In the experiment, ten iron ore granules with different sizes of each moisture group were respectively compressed using a compression test machine (Shimadzu Autograph, AGS Model D). An iron ore granule of known size was placed onto the static plane of the test machine. Then a load piston moved downward and compressed the granule at the speed of 1.0 mm/min. During this period, the compression force  $F_c$  as a function of granule indentation  $\delta$  was recorded. As shown in Fig. 2, the  $F_c$ – $\delta$  curve successively experienced elastic, plastic and fracture regions as compression time increased. To identify the elastic region, we first used a very short compression time after which the load was immediately released. The indentation would decrease back to zero (or to a very small value) if the deformation was in elastic range. With the loading time gradually increasing, a critical indentation which was considered as the threshold

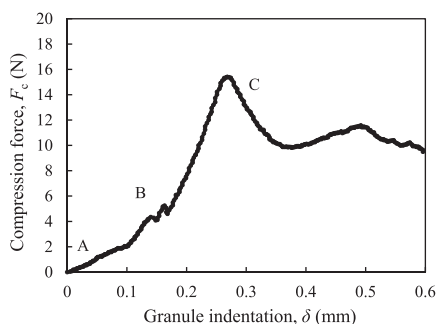


Fig. 2. Example  $F_c$ – $\delta$  curve of an iron ore granule (Granule type A, target moisture 9.5 wt.%, granule size 10.5 mm) in the Young’s modulus measurement test. A: elastic region; B: plastic region; C: fracture region.

of plastic deformation could be found. Based on the data summary, the critical indentation of the studied granules generally ranged from 0.3% to 0.7% of granule diameter.

Based on the data in the elastic region of the  $F_c$ – $\delta$  curve, the elastic modulus of the tested granule could be estimated by the Hertz contact equation given by:

$$F_c = \frac{4}{3} E^* \sqrt{R} \delta^{\frac{3}{2}} \dots (3)$$

where  $F$  is the compression force (N),  $\delta$  is the granule indentation (m),  $R$  is the radius of the sample granule (m) and  $E^*$  is the effective elastic modulus of the sample granule and the load piston (Pa), which is given by:

$$\frac{1}{E^*} = \frac{1 - \sigma_{gran}^2}{E_{gran}} + \frac{1 - \sigma_{pis}^2}{E_{pis}} \dots (4)$$

where  $\sigma_{gran}$  and  $\sigma_{pis}$  refer to the Poisson ratios of the sample granule and the load piston, respectively. Finally, an average Young’s modulus of the ten tested granules of each moisture group was obtained and used for data analysis.

**3.5. Static and Rolling Friction Coefficients between Iron Ore Granules**

The coefficient of the static friction between iron ore granules was estimated by measuring the critical angle of a flat plate that initiated the sliding motion of the granule placed on it. The plate used in the experiment was evenly coated with fine iron ore granules (< 0.5 mm) to mimic the texture of the granule’s surface. These fine granules were collected from the same moisture group with the tested granule. To prevent granule’s rolling down the plate, three individual granules of similar size, as proposed by Pohlman *et al.*<sup>31)</sup> were bonded together with adhesive into a granule tripod set. For each moisture group, ten tripod sets with different average granule sizes were prepared. The tripod set was first placed onto the plate in a horizontal position. Then the plate was tilted at a very low angular velocity until the tripod started sliding. This critical angle that induced the sliding motion was measured by an inclinometer. For each tripod set, the test was repeated five times. Hence, the average static friction coefficient of each tripod set was calculated as

$$\bar{\mu}_s = \frac{1}{5} \sum_{i=1}^5 \tan \theta'_{s,i} \dots (5)$$

where  $\bar{\mu}_s$  is average static friction coefficient of each tripod set and  $\theta'_{s,i}$  is the critical angle measured in the  $i$ th test.

The coefficient of the rolling friction between iron ore granules was measured using the similar method. For each moisture group, twenty individual iron ore granules with different sizes were prepared. In each test, a single granule was put on the plate coated with the fine granules (< 0.5 mm) collected from the same moisture group as the tested granules. As the plate tilted, the critical angle at which the tested granule began rolling was measured. For each tested granule, the measurement was repeated five times. Hence, the average rolling friction coefficient of each granule was calculated as

$$\bar{\mu}_r = \frac{1}{5} \sum_{i=1}^5 \tan \theta'_{r,i} \dots (6)$$

where  $\bar{\mu}_r$  is the average rolling friction coefficient of each tested granule and  $\theta'_{r,i}$  is the critical angle measured in the  $i$ th test.

**4. Results and Discussion**

**4.1. Analysis of Mass Ratio of Adhering Layer to Nuclei Particles**

Figure 3 shows the measurement results of the average mass ratio of adhering layer to nuclei particles of the six granule size fractions,  $\bar{R}_m$ , as a function of moisture content.

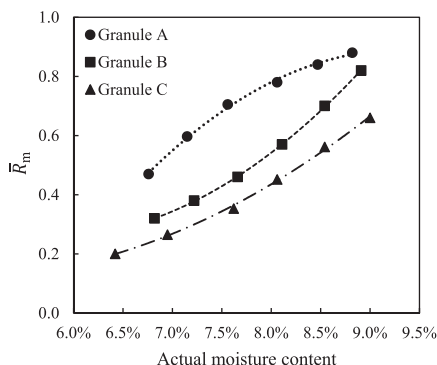


Fig. 3. Average mass ratio of adhering layer to nucleus particle as a function of granule moisture content.

The data indicate that for all granule types,  $\bar{R}_m$  increased significantly with granule moisture content. This upward trend is supposed to be the result of the increasing binding forces between the nuclei and adhering particles as moisture content increased, because in iron ore granulation the major cohesive forces holding the particles together are the capillary forces due to the presence of moisture. During the granulation process, based on the two-stage auto-layering mechanism,<sup>32)</sup> the fine (mainly ultra-fine) particles first layer onto the larger nuclei particles to form an inner adhering layer. Subsequently, the intermediate particles start to get incorporated into the layer through a number of inter-particle collisions,<sup>33)</sup> which continues the growth of the adhering layer. Therefore, the added moisture plays an important role in the growth of the adhering layer of iron ore granules.

Figure 3 also shows that within the lower moisture range ( $W_{MC} \leq 7.5$  wt.%), Granule A has a larger  $\bar{R}_m$  and also a steeper increasing trend of  $\bar{R}_m$  than Granules B and C. This is because under the same lower moisture condition, Ore A, due to its lower porosity ( $P_A = 0.212$  as shown in Table 2) and high mass fraction of  $-0.25$  mm particles ( $w_{-0.25,A} = 16.9$  wt.% as shown in Table 1), could have more moisture available for an effective granulation than the other two ore types. With the moisture content further increasing, the layer growth of Granule A gradually reaches a limit due to the breakage of oversize granules during the granulation process while Granules B and C speed up their growths with increasing amount of available moisture. For the comparison between Granules B and C, Granule C has a slightly lower  $\bar{R}_m$  and less steep trend, especially at higher moisture contents, although the particle porosity of Ore C ( $P_C = 0.235$ ) is lower than the value of Ore B ( $P_B = 0.250$ ). This is mainly because of the different ore size distributions. Compared with Ore B, Ore C has a lower mass fraction of  $-0.25$  mm fines ( $w_{-0.25,B} = 20.3$  wt.%,  $w_{-0.25,C} = 5.7$  wt.%) which constitute the main part of the adhering layer. Therefore, its granulation effectiveness is relatively lower than Ore B at the same moisture content.

Figure 4(a) shows the variation in mass ratio of adhering layer to nuclei particles,  $R_m$ , as a function of granule size for the granules at the optimal moisture content. The data illustrate that for all the granule types at the optimal moisture contents,  $R_m$  increased first and then decreased with the granule size, presenting a maximum value in the parabolic-like trend. This trend results from the combination of the different rates of growth of the adhering layer and nuclei particle size as granule size increases. As the granule size increases within the lower range, there are more adhering fines incorporated into the layer around these granules due to the higher granule momentum and better inter-granule contact conditions, which consequently result in the ascending trend of the curve  $R_m$ . However, as the granule size further increases, the layer growth of these granules gradually slows down because the particles (mainly intermediate particles) attached onto the surface of the adhering layer more

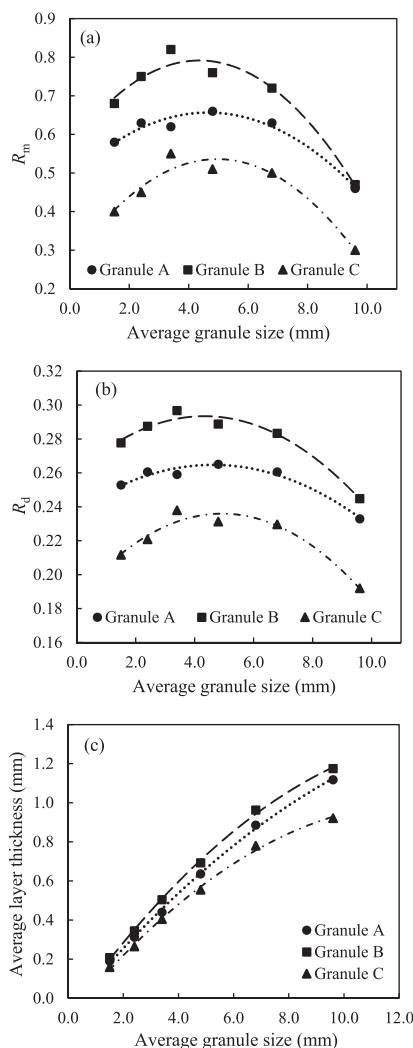


Fig. 4. Data of adhering layer as a function of granule size for the granules at the optimal moisture content. (a) layer mass/nuclei mass; (b) layer thickness/nuclei radius; (c) average layer thickness. The average granule size refers to the geometric mean size of each size fraction.

easily get detached due to the increasing tangential shear force as granule size increases. On the other hand, the mass of nuclei particles keeps increasing with the nuclei particle size at a cubic rate ( $m-d^3$ ). As a result, the mass ratio of the adhering layer to the nuclei particles  $R_m$  starts to present a decreasing trend.

Under the assumption that both the granules and nuclei particles are spherical,  $R_m$  could be converted into the ratio of layer thickness to granule radius,  $R_d$ :

$$R_d = 1 - \frac{1}{\sqrt[3]{(1 + R_m) \cdot \left(\frac{\rho_N}{\rho_a}\right)}} \dots\dots\dots (7)$$

where  $\rho_N$  and  $\rho_a$  are the average apparent densities of the nuclei particles and iron ore granules of each type, respectively. Furthermore, the average adhering layer thickness of each granule size fraction could be estimated by the product of  $R_d$  (as shown in Fig. 4(b)) and the geometric mean granule radius of each granule size fraction. (The geometric mean granule size of  $+8.0$  mm was determined as the average of  $8.0$  mm and  $11.2$  mm). The calculated results, as shown in Fig. 4(c), illustrate that the average adhering layer thickness increased with granule size, which indicate that at the optimal moisture content, larger granules normally have a thicker adhering layer than the smaller ones. This trend

nearly agrees with the assumption proposed by Litster *et al.*<sup>3)</sup> that layer thickness is proportional to nuclei particle size if the mass ratio  $R_m$  is constant. However, based on the measurement results,  $R_m$  is actually not independent on the granule size. This is the reason why the fitting curves in Fig. 4(c) are not linear trendlines. The curve of Granule A is close to linear because Granule A has a relatively constant  $R_m$  as shown in Fig. 4(a).

#### 4.2. Analysis of Granule Sphericity

The average sphericity of iron ore granules as a function of moisture content is shown in Fig. 5. The data indicate that for all three granule types, the average granule sphericity increased with moisture content. The main reason for the ascending trend of granule sphericity with moisture is that with increasing moisture, the nuclei particles were coated with a thicker adhering layer (as shown in Fig. 4). Under the tumbling effect during the granulation, the resultant granules generally ended up with a higher sphericity. The order of the sphericity between the granule types ( $\phi_C > \phi_A > \phi_B$ ) is largely affected by the sphericity of the nuclei particles of the iron ore types. The ore type having a higher sphericity of nuclei particles usually resulted in the corresponding granule type with a higher sphericity.

The relationship between the granule sphericity and granule size at the optimal moisture level is shown in Fig. 6. Based on the measurement data, it can be seen that the granule sphericity slightly increased with granule size. The reason for the upward trend lies in the advantage of the larger nuclei particles in attaching fine and intermediate particles, due to their higher momentum,<sup>3)</sup> over the smaller nuclei particles. As a result, the larger granules ended up with a relatively thicker adhering layer, as shown in Fig. 4(c). However, as the moisture content reached the optimal level, this advantage had become less significant. This is because with proper moisture addition, most smaller granules could be also coated with a relatively complete adhering layer like

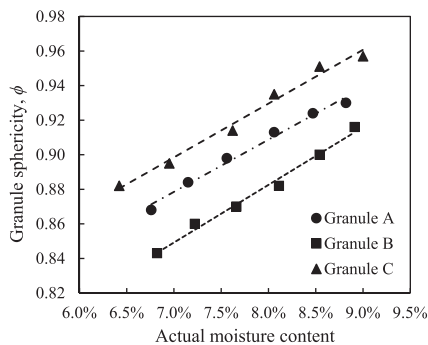


Fig. 5. Average sphericity of iron ore granules as a function of moisture content.

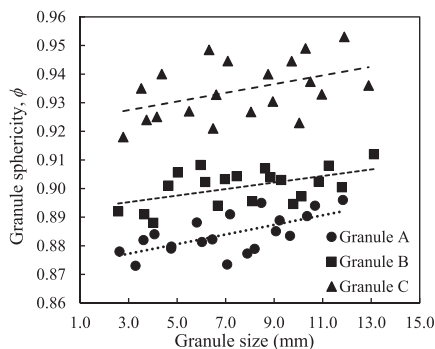


Fig. 6. Sphericity of the iron ore granules at the optimal moisture content as a function of granule size.

the larger ones. Therefore, the granule sphericity gradually became independent of granule size, which explained the low slope of the upward trend in Fig. 6.

#### 4.3. Analysis of Apparent Density

The measurement results of the apparent density of iron ore granules with full size distribution are summarised in Fig. 7(a). The data indicate that the apparent density generally decreased with the increase of moisture content. The thickness of the adhering layer, as mentioned in Section 4.1, is strongly dependent on the amount of the available moisture present on the ore particle surface. With more water added, the increasing binding forces lead to a higher chance of incorporating the intermediate particles to the layer. The density of the adhering layer, due to its highly porous structure, is normally lower than value of nuclei particles. Therefore, the apparent density of the iron ore granules, assuming the layer porosity is constant, generally decreases with the mass ratio of layer to nuclei particles. Note that although the  $\bar{R}_m$  of Granule A is larger than the values of Granules B and C at the same moisture content (as shown in Fig. 3), the average apparent density of Granule A is still larger than the values of Granules B and C over the studied moisture range. This is because Ore A has a higher apparent density ( $3.76 \text{ g/cm}^3$ ) than Ore B ( $3.38 \text{ g/cm}^3$ ) and Ore C ( $3.05 \text{ g/cm}^3$ ), as is shown in Table 2. Therefore, it can be seen that the apparent density of iron ore granules  $\rho_a$  is a complex parameter which is not only related to  $\bar{R}_m$  but also significantly dependent on the density of the raw ore particles.

Figure 7(a) also shows that the downward trend slope of the apparent density varies with the granule types. This is mainly because of the different particle characteristics, *e.g.* porosity, sphericity and size distribution, between iron ore types. With the increase of added moisture, the difference in the porosity of nuclei particles affects the trends in the available moisture for granulation. The ore type having a lower porosity (*e.g.* Ore A) can utilise a larger amount of available moisture for granulation at lower moisture contents and

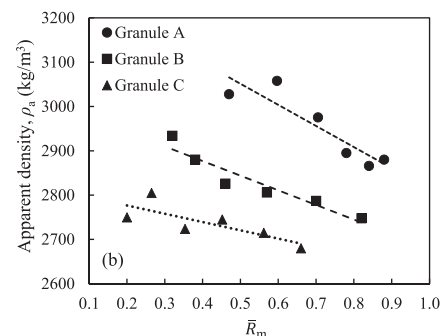
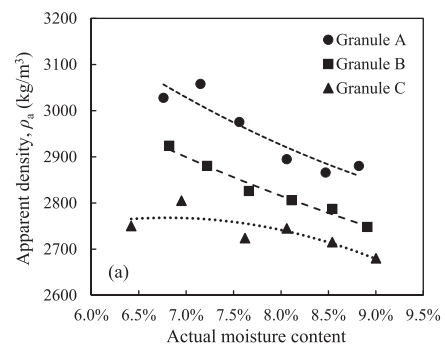


Fig. 7. Apparent density of the iron ore granules with full size distribution as a function of (a) actual moisture content; (b)  $\bar{R}_m$ .

thus has a faster growth rate of adhering layer. As moisture further increases, its granulation effectiveness gradually reaches a balance while the ore with a higher porosity (e.g. Ore C) starts the fast rate granulations with more available moisture. In addition to porosity, particle shape also affects the layer growth rate with increasing moisture content. The present commonly-accepted proposal<sup>34,35</sup> is that irregularly shaped and rough particles are good nuclei, with a higher chance of attaching fine and intermediate particles onto granule layers. In summary, the overall effects of these ore particle characteristics on the growth of adhering layer result in the different trend slopes of the apparent density between the studied granule types. In addition, a general correlation between  $\rho_a$  and  $\bar{R}_m$  is shown in Fig. 7(b).

The apparent density of the iron ore granules at the optimal moisture content as a function of granule size is shown in Fig. 8. The data show that the apparent density varied between the granule size fractions and the trends were also different between the granule types. This is probably due to the heterogeneous nature of the raw material mixture used in the granulation. Due to the different size distributions of the mixture components (as shown in Fig. 9), the overall composition of the iron ore granules of each size fraction is not constant. For instance, the components with a relatively lower density (e.g. fluxes or coke breeze) may have a higher chance of acting as nuclei particles in one size fraction, which would decrease the average apparent density of the iron ore granules of the corresponding size range. In turn, a larger fraction of iron ore or return sinter particles acting as nuclei in one size fraction would result in an increased average apparent density of the corresponding iron ore granules. In general, the reasons for the difference of the average apparent density between size fractions are quite complex. Further experimental studies are needed for a clear explanation.

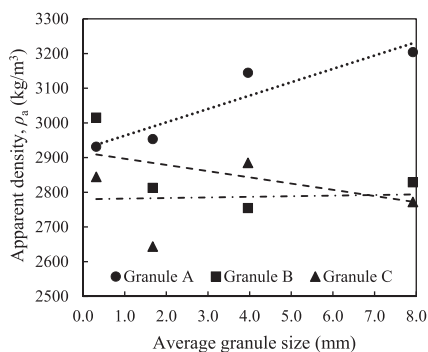


Fig. 8. Apparent density of the iron ore granules at the optimal moisture content as a function of granule size. The average granule size refers to the geometric mean size of each size fraction.

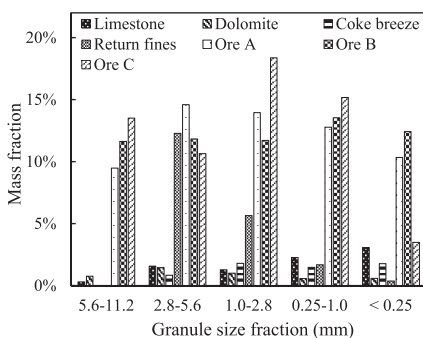


Fig. 9. Summary of the mixture component size distributions based on the data shown in Tables 1, 3 and 4.

#### 4.4. Analysis of Young's modulus

Figure 10 shows the measurement results of average Young's modulus of iron ore granules as a function of moisture content. The data indicate that for all three granule types, the Young's modulus of iron ore granules generally decreased with the moisture content. The reason is probably that at lower moisture contents, the nuclei particles, as is shown in Fig. 3, were coated with a relatively thinner adhering layer. In particular for some nuclei particles with a high porosity, they were probably only coated with a thin layer of ultrafine particles. The granules with such a structure generally have a relatively higher Young's modulus. As moisture increased, the layer thickness gradually increased. This made the granules softer and more deformable since the capillary forces holding the particles together were relatively weak. Hence, the Young's modulus of the granules decreased.

Compared with Granules A and B, the average Young's modulus of Granule C was higher over the moisture range. This is because Ore C has relatively lower adhering fines smaller than 0.25 mm but higher nucleus component larger than 1.0 mm (as shown in Table 1). Therefore, the nuclei particles were coated with fewer fine particles compared with those of Ores A and B, and thus the resultant granules had a relatively thinner adhering layer. This comparison is also shown in Fig. 4. Compared with Granules B and C, Granule A had a less steep downward trend at the higher moisture contents. This is probably because compared with Granules B and C, Granule A already had a relatively complete and stable adhering layer within the first half of the moisture range ( $W_{MC} \leq 7.5$  wt.%). As moisture content further increased, the growth of the adhering layer for Granule A gradually reached an equilibrium<sup>3,33</sup> in which there was balance between the incorporation and detachment of the fine and intermediate particles via interparticle collisions. Therefore, the layer growth gradually slowed down and the layer thickness became constant. As a result, the Young's modulus of granules also reached a relatively stable state. Similar to Granule A, for Granules B and C there may also exist a corresponding moisture content at which the slope of the curve starts to change obviously, however, this is likely to occur at higher moisture contents because of their relatively higher water holding capacity (WHC).

The measured Young's modulus of the iron ore granules at the optimal moisture contents as a function of granule size are shown in Fig. 11(a). The data indicate that for each granule type, the Young's modulus showed a general downward trend with the increase of granule size. This downward trend is because the smaller granules normally had a relatively thinner adhering layer, as shown in Fig. 4(c), and thus were not as deformable as the larger ones. Figure 11(b) presents the relationship between the Young's modulus of the iron ore granules at the optimal moisture and the adhering layer thickness. This relationship was obtained based on the data shown in Figs. 4(c) and 11(a). The trend indicates that as

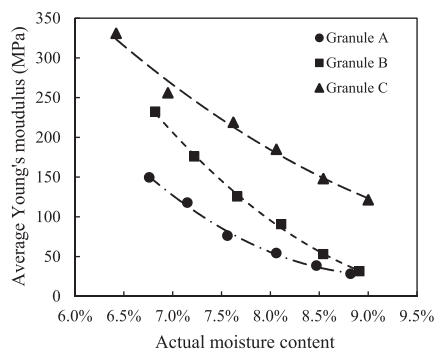


Fig. 10. Average Young's modulus of iron ore granules as a function of moisture content.

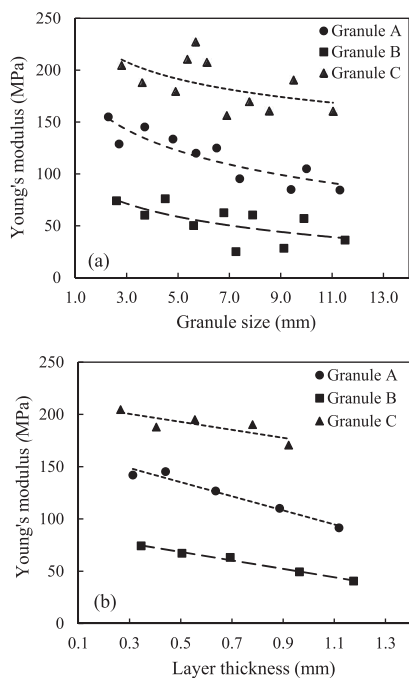


Fig. 11. Young's modulus of the iron ore granules at the optimal moisture content (a) as a function of size; (b) as a function of layer thickness.

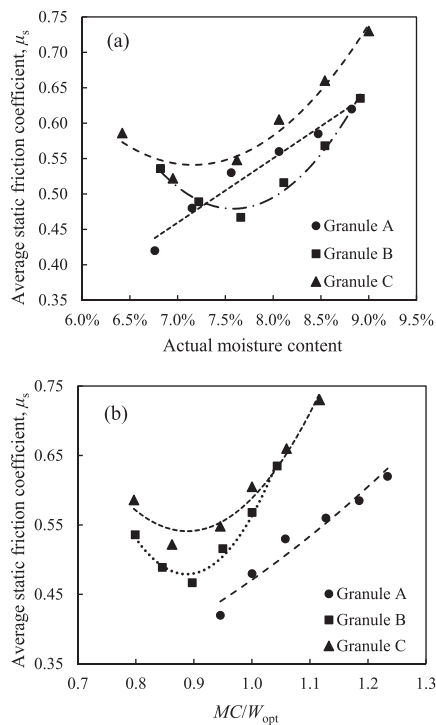


Fig. 12. Average static friction coefficient of iron ore granules as a function of (a): actual moisture content; (b)  $MC/W_{opt}$ .

the thickness of the granule adhering layer increased, the Young's modulus showed a similar downward trend to the one shown in Fig. 11(a).

4.5. Analysis of Static Friction Coefficient

The measurement results of the average static friction coefficient of iron ore granules as a function of moisture are shown in Fig. 12(a). Based on the data, it can be seen that the friction coefficient of Granule A has a linear trend with the moisture content while for Granules B and C, the corresponding trends are parabolic. The reason for the upward trend of Granule A is probably that as the available moisture content increased, more intermediate particles were incorporated into the adhering layer due to the increase of capillary forces, which could effectively coarsen the granule surface. Furthermore, increasing moisture also led to the increase of the adhesive force<sup>36)</sup> between the particles attached on the granule surface and the testing plate surface, which also contributed to the increase of the apparent static friction coefficient. For Granules B and C, the average static friction coefficient first showed a higher value at the lower moisture contents because a large proportion of granules were still poorly coated with a discontinuous adhering layer due to the high porosity of their nuclei particles. The surface of these granules was relatively rougher than their counterparts of Granule A. As moisture increased, the adhering layer gradually thickened from hardly covering the nuclei particle to incorporating enough adhering fines into the growing layer. Similar to Granule A, as a result of the coarsening of granule surface and the increase of adhesion, the average static friction coefficients of Granules B and C increased with moisture content.

The positions of the turning points of the parabolic curves shown in Fig. 12(a) are assumed to be related to the properties of granule types. To prove this assumption, the static friction coefficients  $\mu_s$  are plotted as a function of the ratio of moisture content to the optimal moisture content ( $MC/W_{opt}$ ) for the three granule types as shown in Fig. 12(b). It is noticeable that the minima in the curves for Granules B and C occur at a  $MC/W_{opt}$  of around 0.9. By testing all of the iron ores over the same moisture range, the Granule A samples

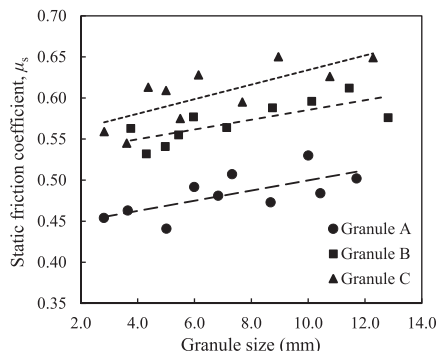


Fig. 13. Static friction coefficient of iron ore granules at the optimal moisture content as a function of granule size. Granule size refers to the average diameter of the three granules comprising the tripod set.

did not reach a sufficiently low value of  $MC/W_{opt}$  to exhibit a minimum. However, it is assumed that this would also occur for Granule A at a similar position to Granules B and C.

The relationships between the static friction coefficient and granule size at the optimal moisture levels are shown in Fig. 13. The results indicate that for all the granule types, the static friction coefficients slightly increased with a smaller slope. The upward trend was attributed to the difference of the adhering layer thickness between the smaller and larger granules, as mentioned in Section 4.1. However, as the moisture content reached the optimal level, the smaller granules started to incorporate some intermediate particles onto their adhering layers as well. Hence, the surface roughness of the smaller granules became close to the value of the larger ones, which explained the low slope of the upward trend in Fig. 13.

4.6. Analysis of Rolling Friction Coefficient

The measurement results of the average rolling friction coefficient as a function of granule moisture are shown in

**Fig. 14(a).** For all three granule types, the data show the parabolic-like trends in which the rolling friction coefficient first decreased and then increased with moisture content. The descending part of the trend is probably because of the increase of granule sphericity with increasing moisture content, as is shown in Fig. 5. The increase of granule sphericity may effectively decrease the rolling resistance acting on the granules. The ascending part of the trend is probably because of the increased adhesive force between the granule surface and the plate surface with increasing moisture content. The increase of adhesion enhanced the rolling resistance acting on the granules.<sup>37,38)</sup> Based on the above considerations, it is assumed that at lower levels of moisture, the increase in granule sphericity was the main reason that contributed to the decrease in rolling resistance. With the increase of moisture, this effect was being opposed by the increase of adhesive force. At the higher moisture contents, the influence of adhesive force was thought to be dominant and the net effect caused rolling friction coefficient to increase.

Due to the different particle characteristics between the ore types, the position of the turning point of the trend for each granule type is different. Similar to the moisture content normalisation for the static friction coefficient  $\mu_s$  as shown in Fig. 12(b), the rolling friction coefficients  $\mu_r$  for the three granule types are also plotted as a function of  $MC/W_{opt}$  as shown in Fig. 14(b). The minimum of each curve occurs at a similar value of  $MC/W_{opt}$  (between 1.0 to 1.1), suggesting that the shape of the  $\mu_r$  curve is also largely dependent on the optimal moisture content  $W_{opt}$  of iron ore granule types. Furthermore, it is anticipated that the  $MC/W_{opt}$  at the minima of the curves for  $\mu_s$  and  $\mu_r$  would occur at a value of around 1.0, although the specific values for the cases of  $\mu_s$  and  $\mu_r$  are slightly different. The difference in the location of the minima is attributed to differences in the competing mechanisms in each case. Firstly, regarding  $\mu_s$ , we believe the parabolic curve shown in Fig. 12 is mainly due to the competing mechanisms of 1) changing granule surface roughness due to the growth of the adhering

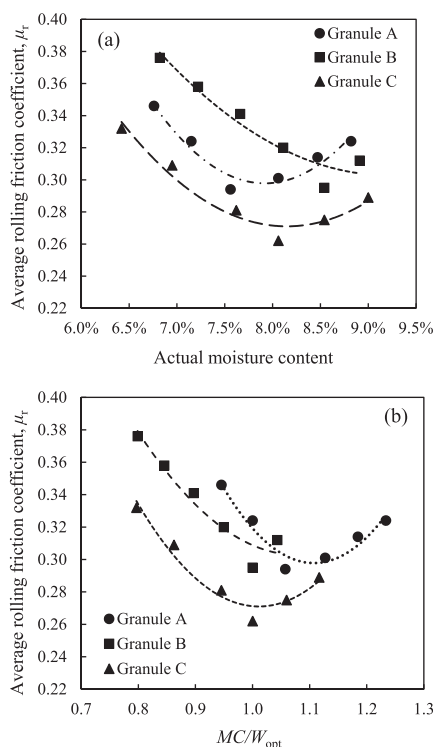


**Fig. 14.** Average rolling friction coefficient between iron ore granules as a function of (a): actual moisture content; (b)  $MC/W_{opt}$ .

layer and 2) the increase in the inter-granule adhesive force with increasing moisture content. As the moisture content increased within the lower range the nuclei particles, which were irregular in shape, were gradually coated by more fine particles and thus the resultant granule surface became smoother. As the moisture content further increased, the capillary forces became larger and, as a result, an increasing number of intermediate particles attached to the adhering layer of the granules. With more intermediate particles attached, the granule surface became rougher. At the same time, we assume that the inter-granule adhesive force increased with increasing moisture content. Therefore, due to interaction of these two mechanisms, the resultant curve of  $\mu_s$  is obtained as shown in Fig. 12.

Secondly, regarding  $\mu_r$ , the parabolic curve shown in Fig. 14 is mainly due to the competing mechanisms of 1) the increase in granule sphericity and 2) increase in the inter-granule adhesive force with increasing moisture content. As the moisture content increased in the low range the increase in granule sphericity was dominant and contributed to the decrease in  $\mu_r$ . As moisture content further increased to about 1.0–1.1 times of  $W_{opt}$ , the inter-granule adhesive force increased significantly, finally resulting an upward trend of  $\mu_r$  at the higher moisture contents.

The relationships between the rolling friction coefficient and granule size at the optimal moisture levels are shown in Fig. 15. The measurement data of all three granule types generally show that the rolling friction coefficient does not strongly depend on the granule size and shows a slight downward trend over the considered size range. This is because at the optimal moisture contents, the granule sphericity, as shown in Fig. 6, had become nearly independent of granule size and showed a slight upward trend over the size range.

**4.7. Discussion of the Impact of Granule Size**

The granules for each ore type generally increase in size with increasing moisture content as expected (Fig. 16(a)), with a decreasing proportion of granules with a size smaller than 1 mm (Fig. 16(b)). Where possible, granule properties were measured for the full size distribution of granules, however, for a number of measurement techniques (e.g. mass ratio of adhering layer to nuclei particles, granule sphericity and Young’s modulus, etc.), it was not possible to obtain accurate measurements for the  $-1$  mm size fraction. It is acknowledged that this size fraction has a non-negligible impact on the permeability of the sinter bed, however, at  $W_{opt}$  the proportion of these granules is small (as shown by the underlined points in Fig. 16(b). In most cases the granule properties are not a strong function of granule size (e.g. granule sphericity, Young’s modulus and the coefficients of static and rolling frictions) and the properties of small granules could be extrapolated from the measured data if required.

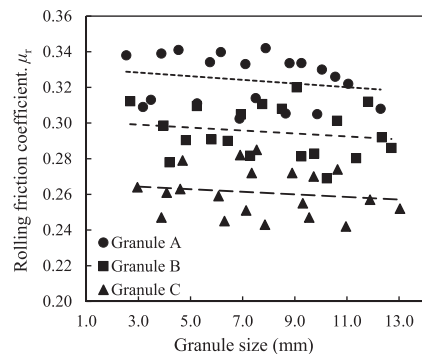


**Fig. 15.** Rolling friction coefficient of the iron ore granules at the optimal moisture content as a function of granule size.

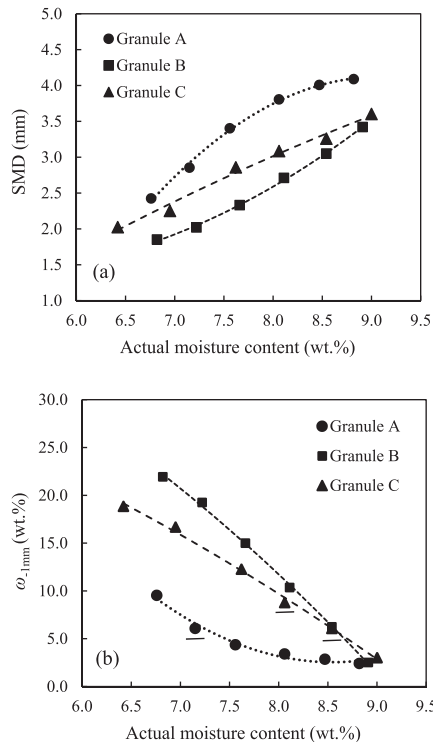


**Fig. 16.** (a) SMD and (b) the mass fraction of  $-1$  mm granules as a function of moisture content for each iron ore granule type.

## 5. Conclusions

Some key property parameters, including apparent density, Young's modulus and the coefficients of static and rolling frictions, of the iron ore granules made from three types of single Australian iron ores were measured. The relationship between each parameter and moisture content was examined. The variation in each parameter with granule size was also investigated at the optimal moisture content for each granule type. The conclusions obtained are as follows:

(1) The apparent density of iron ore granules generally decreased with moisture content for all granule types. The slope of the downward trend varied with granule types due to the different particle characteristics between the ore types. The apparent density varied between granule size fractions since the overall composition of the iron ore granules of each size fraction is not constant.

(2) The Young's modulus of iron ore granules generally decreased with moisture content. The ore type with a coarser size distribution tended to generate granules with a higher Young's modulus. At the optimal moisture content, the Young's modulus showed a slight downward trend with granule size.

(3) Within the considered moisture range, the static friction coefficient of Granule A presented a monotonously increasing trend while for Granules B and C, their static friction coefficients experienced a minimum value as moisture content increased. At the optimal moisture content, the static friction coefficients increased slightly with granule size.

(4) The rolling friction coefficient went through a minimum value as moisture content increased. The moisture content corresponding to the minimum value varied with granule type due to the different particle characteristics of

the ore types. At the optimal moisture content, the rolling friction coefficient was nearly independent of granule size.

## Acknowledgements

The authors gratefully acknowledge the China Scholarship Council as well as the Australian Research Council in supporting the ARC Research Hub for Advanced Technologies for Australian Iron Ore. The authors are also thankful to BHP for financial support and permission to publish the paper.

## REFERENCES

- 1) USGS: *Min. Eng.*, **69** (2017), 20.
- 2) C. E. Loo: *ISIJ Int.*, **45** (2005), 436.
- 3) J. D. Litster, A. G. Waters and S. K. Nicol: *Trans. Iron Steel Inst. Jpn.*, **26** (1986), 1036.
- 4) P. C. Kapur, P. Kapur and D. W. Fuerstenau: *Int. J. Miner. Process.*, **39** (1993), 239.
- 5) J. D. Litster and A. G. Waters: *Powder Technol.*, **55** (1988), 141.
- 6) J. P. Zhao, C. E. Loo and B. G. Ellis: *ISIJ Int.*, **56** (2016), 1148.
- 7) L. Lu and O. Ishiyama: *Trans. Inst. Min. Metall. C*, **125** (2016), 132.
- 8) D. Fernández-González, I. Ruiz-Bustinza, J. Mochón, C. González-Gasca and L. F. Verdeja: *Miner. Process. Extr. Metall. Rev.*, **38** (2017), 36.
- 9) M. V. Ramos, E. Kasai, J. Kano and T. Nakamura: *ISIJ Int.*, **40** (2000), 448.
- 10) J. Kano, E. Kasai, F. Saito and T. Kawaguchi: *ISIJ Int.*, **45** (2005), 500.
- 11) R. Soda, A. Sato, J. Kano, E. Kasai, F. Saito, M. Hara and T. Kawaguchi: *ISIJ Int.*, **49** (2009), 645.
- 12) T. Umekage and S. Yuu: *ISIJ Int.*, **49** (2009), 693.
- 13) M. Nakano, T. Abe, J. Kano and K. Kunitomo: *ISIJ Int.*, **52** (2012), 1559.
- 14) S. Ishihara, R. Soda, Q. Zhang and J. Kano: *ISIJ Int.*, **53** (2013), 1555.
- 15) C. Li, T. Honeyands, D. P. O'Dea and R. Moreno-Atanasio: *Powder Technol.*, **320** (2017), 257.
- 16) A. W. Jenike: *Storage and Flow of Solids*, University of Utah, Salt Lake City, UT, (1964), 1.
- 17) J. F. Carr and D. M. Walker: *Powder Technol.*, **1** (1968), 369.
- 18) G. K. P. Barrios, R. M. d. Carvalho, A. Kwade and L. M. Tavares: *Powder Technol.*, **248** (2013), 84.
- 19) D. Wang, M. Servin, T. Berglund, K.-O. Mickelsson and S. Rönnbäck: *Powder Technol.*, **283** (2015), 475.
- 20) J. Hinkley, A. G. Waters, D. O'Dea and J. D. Litster: *Int. J. Miner. Process.*, **41** (1994), 53.
- 21) A. Doménech, T. Doménech and J. Cebrián: *Am. J. Phys.*, **55** (1987), 231.
- 22) J. Ai, J.-F. Chen, J. M. Rotter and J. Y. Ooi: *Powder Technol.*, **206** (2011), 269.
- 23) H. Wadell: *J. Geol.*, **43** (1935), 250.
- 24) T. Higuchi, L. Lu and E. Kasai: *ISIJ Int.*, **57** (2017), 1384.
- 25) Z. Que, S. Wu, X. Zhai and K. Li: *Ironmaking Steelmaking*, <https://doi.org/10.1080/03019233.2017.1368954>.
- 26) B. G. Ellis, C. E. Loo and D. Witchard: *Ironmaking Steelmaking*, **34** (2007), 99.
- 27) A. M. Nyembwe, R. D. Cromarty and A. M. Garbers-Craig: *Trans. Inst. Min. Metall. C*, **125** (2016), 178.
- 28) H. Zhou, M. X. Zhou, D. P. O'Dea, B. G. Ellis, J. Z. Chen and M. Cheng: *ISIJ Int.*, **56** (2016), 1920.
- 29) M. X. Zhou, H. Zhou, D. P. O'Dea, B. G. Ellis, T. Honeyands and X. T. Guo: *ISIJ Int.*, **57** (2017), 1004.
- 30) H. Hertz: *J. Reine Angew. Math.*, **92** (1882), 156.
- 31) N. A. Pohlman, B. L. Severson, J. M. Ottino and R. L. Lueptow: *Phys. Rev. E*, **73** (2006), 031304.
- 32) P. W. Roller: *BHP Tech. Bull.*, **26** (1982), 44.
- 33) J. D. Litster and A. G. Waters: *Powder Technol.*, **62** (1990), 125.
- 34) A. Formoso, A. Moro, G. F. Pello, J. L. Menéndez, M. Muñiz and A. Cores: *Ironmaking Steelmaking*, **30** (2003), 447.
- 35) M. Gan, X. H. Fan, Z. Y. Ji, X. L. Chen, L. Yin, T. Jiang, Z. Y. Yu and Y. S. Huang: *Ironmaking Steelmaking*, **42** (2015), 351.
- 36) Y. Shimada, Y. Yonezawa and H. Sunada: *J. Pharm. Sci.*, **92** (2002), 560.
- 37) K. Kendall: *Wear*, **33** (1975), 351.
- 38) B. M. Hanrahan, S. Misra, M. I. Beyaz, J. H. Feldman, C. M. Waits and R. Ghodssi: *Tribol. Lett.*, **56** (2014), 215.